Turbulent particle flux to a perfectly absorbing surface

By J. MANN[1], S. OTT[1], H. L. PÉCSELI[2,3]
AND J. TRULSEN[3,4]

[1]Risø National Laboratory, DK-4000 Roskilde, Denmark
[2]University of Oslo, Institute of Physics, Box 1048 Blindern, N-0316 Oslo, Norway
[3]Centre for Advanced Study, Drammensveien 78, N-0271 Oslo, Norway
[4]University of Oslo, Institute of Theoretical Astrophysics, Box 1029 Blindern, N-0315 Oslo, Norway

The feasibility of an experimental method for investigations of the particle flux to an absorbing surface in turbulent flows is demonstrated in a Lagrangian as well as an Eulerian representation. A laboratory experiment is carried out, where an approximately homogeneous and isotropic turbulent flow is generated by two moving grids. The simultaneous trajectories of many small approximately neutrally buoyant polystyrene particles are followed in time. In a Lagrangian analysis, we select one of these as the centre of a 'sphere of interception', and obtain estimates for the time variation of the statistical average of the inward particle flux through the surface of this moving sphere. The variation of the flux with the radius in the sphere of interception, as well as the variation with basic flow parameters is described well by a simple model, in particular for radii smaller than a characteristic length scale for the turbulence. The Eulerian counterpart of the problem is analysed as well, and the two results compared. Applications of the problem to, for instance, the question of the feeding rate of micro-organisms in turbulent marine environments are pointed out.

1. Introduction

Often, the problem of turbulent diffusion in neutral turbulent flows is analysed in terms of an initial value problem (Batchelor 1952; Roberts 1961). However, for many applications, a boundary value problem is more relevant. As such an example we here consider the turbulent particle flux to a perfectly absorbing spherical surface, which is a realistic physical model for many practical applications. This formulation of the problem serves, for instance, as a model for predator–prey encounters in turbulent waters, which seems to be the application that has received most attention recently (Sundby & Fossum 1990; Kiørboe & Saiz 1995). For small predators, fish larvae for instance (Muelbert, Lewis & Kelley 1994), it can be assumed that their self-induced motion is small or negligible, and that they are passively convected by the local flow velocity, at least to a good approximation. Similarly, it can be assumed that their food (micro-zooplankton, for instance) is also passively convected by the same flow. The feeding process can be modelled by assuming that any individual prey entering a suitably defined 'sphere of interception' is captured with certainty. The surface is thus 'virtual' in the sense that it does not disturb the flow.

In turbulent waters, the prey flux to a passively convected predator is related to the problem of relative diffusion, but now considered as a boundary value problem, with
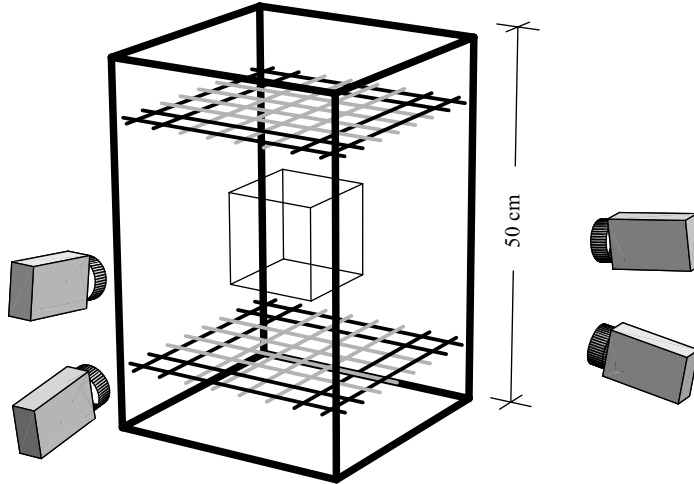
FIGURE 1. Schematic illustration of the experimental set-up, showing the movable grids and the four video cameras. A restricted measuring volume of $140 \times 140 \times 120 \, \text{mm}^3$ is shown by thin lines.

the sphere of interception acting as a perfect absorber of prey. This is the standard model for this particular problem (Rothschild & Osborn 1988; Osborn 1996). We use this as a reference case in the following, for simplicity and definiteness. The general interest in the problem arises essentially from the simple observation that the food concentration in the near region of a predator will rapidly be depleted, and without any self-induced motion a predator starve, unless the prey within its sphere of interception is replaced by turbulent mixing in the surrounding flow. Although the results presented in this work explicitly refer to spherical volumes, the scaling laws that are obtained will have a wider range of applications.

We propose and demonstrate the feasibility of an experimental method for a quantitative study of turbulent transport into an absorbing surface, and present results for varying parameters. It is demonstrated that a relatively simple model equation is adequate for describing the basic features of our observations. The paper is organized as follows. In §2 we give a short summary of the experimental set up, and the experimental conditions. In §3 we analyse the simplest problem for the turbulent flux to a *stationary* spherical surface. In §4 we discuss experimental results for particle fluxes to an absorbing sphere where the centre is identified by a particle which is moving with the flow. Section 5 contains a discussion of a simple analytical model which gives results in fair agreement with observations. Finally, §6 contains our conclusions. Preliminary results from our study were published in Mann *et al.* (2002). Some of the figures in the following sections show normalized fluxes: the appropriate normalizing quantity is stated explicitly in each case.

2. Experimental set-up

The basic features of the present experiment are described elsewhere (Ott & Mann 2000), with a detailed description given by Mann, Ott & Andersen (1999). A short summary will suffice here. The turbulence is generated by the motion of two plastic grids, near the top and bottom of a tank with $320 \times 320 \times 450 \, \text{mm}^3$ inner dimensions, see figure 1 for a schematic illustration.

$\alpha\epsilon^{2/3}$ $(\mathrm{mm^{4/3}\,s^{-2}})$	$\mathscr{L}_E$ (mm)	σ $(\mathrm{mm\,s^{-1}})$	$\mathscr{L}_{\mathrm{int}}$ (mm)	ϵ $(\mathrm{mm^2\,s^{-3}})$	τ_η (s)	η (mm)	λ (mm)	R_λ
45	31	18	23	160	0.075	0.26	5.1	100
41	27	16	20	140	0.080	0.27	4.9	88
40	29	16	22	135	0.081	0.27	5.1	93
45	28	17	21	160	0.075	0.26	4.9	91
24	29	12	22	62	0.120	0.33	5.8	81
65	29	21	22	279	0.056	0.22	4.5	104
56	28	19	21	225	0.063	0.24	4.6	97
25	27	12	20	65	0.117	0.32	5.6	78

TABLE 1. Summary of the parameters derived from the second-order structure function and the spectra obtained from it, based on measurements in the restricted volume shown in figure 1.

Typical Taylor micro-scale Reynolds numbers (Hinze 1975), $R_\lambda = \lambda^2/(\eta^2\sqrt{15})$, are ~ 100 for the present conditions, using the Taylor micro-scale $\lambda = \sqrt{15\nu\sigma^2/\epsilon}$, where $\nu \simeq 0.89\,\mathrm{mm^2\,s^{-1}}$ is the kinematic viscosity of the water, ϵ is specific energy dissipation rate, and σ^2 is the variance of one velocity component. The Kolmogorov length scale $\eta = (\nu^3/\epsilon)^{1/4}$ is less than $1/2\,\mathrm{mm}$ for the present conditions, while Kolmogorov time scales τ_η are in the range 0.05–$0.12\,\mathrm{s}$. The 'micro-scale' η represents the length scales where the viscous effects become important. A characteristic Eulerian length scale ('outer' scale) $\mathscr{L}_E$ as well as ϵ are determined by fitting a von Kármán type wavenumber spectrum (Mann *et al.* 1999; Ott & Mann 2000) to the experimentally obtained data,

$$E(k) = \alpha\epsilon^{2/3}\mathscr{L}_E^{5/3}\frac{(\mathscr{L}_E k)^4}{(1+(\mathscr{L}_E k)^2)^{17/6}}, \qquad (2.1)$$

where α is the spectral Kolmogorov constant (Monin & Yaglom 1975). $\mathscr{L}_E$ is found to be in the range 25–$30\,\mathrm{mm}$. We can interpret $\mathscr{L}_E$ as the lower limit for separations between fixed frame detection points, where the velocities of fluid elements tend to become uncorrelated. As a working hypothesis we can assume that velocities are also statistically independent for separations larger than $\mathscr{L}_E$. An integral length scale can be defined by the integral of the parallel velocity-component correlation function $R_\parallel(r)$ as $\mathscr{L}_{\mathrm{int}} = \int_0^\infty R_\parallel(r)\,\mathrm{d}r$. A summary of parameters for eight different conditions used in the present work is given in table 1.

The motions of small polystyrene particles of size $a = 0.5$–$0.6\,\mathrm{mm}$ are followed with four video-cameras, and the simultaneous positions of typically 500–1000 particles recorded at time intervals of $1/25\,\mathrm{s}$. The size of the effective measuring volume is approximately $140 \times 140 \times 120\,\mathrm{mm^3}$. It is ensured that the particles used in the experiment are approximately neutrally buoyant, as described by Mann *et al.* (1999). By a tracking procedure it is then possible to link the positions of particles (Mann *et al.* 1999), and thus follow their individual motions in three spatial dimensions. In particular their time varying velocity can also be deduced. An illustrative sample trajectory is shown in figure 2, showing a series of small spheres, centred at the particle positions, at individual sampling times. For illustration, the spheres are here drawn much larger than the polystyrene particles. The reference particle moves in the downward direction. Since this time sequence is one of the longer ones obtained, the superposition of the spheres at subsequent sampling times gives rise to an appearance like a grey 'band'.
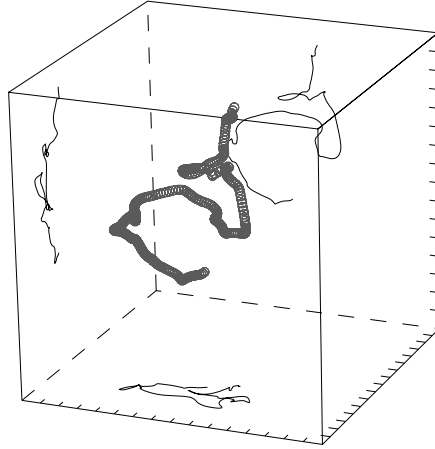
FIGURE 2. Sample of particle trajectory obtained experimentally with $1/25$ s time resolution. The small spheres give the particle position, and the continuous line is a numerically interpolated particle trajectory, projected onto three of the bounding surfaces of the box. The distance between the tic-marks on axes is 10 mm. Dashed lines show the back side of the figure.
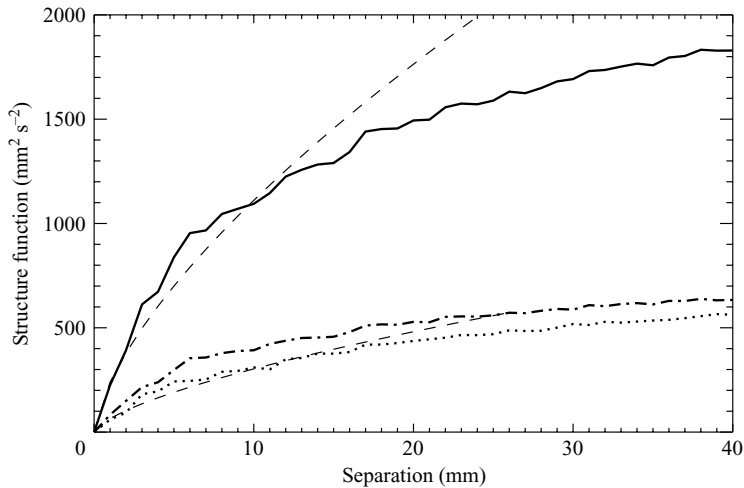

FIGURE 3. Experimentally obtained second-order structure function, as a function of separation variable y. The upper dashed line shows a $y^{2/3}$ fit. The dotted line refers to the longitudinal structure function, and the dot-dashed line to its transverse counterpart. The full line gives the structure function $\Psi_{2\parallel} + 2\Psi_{2\perp}$.

Experiments are carried out for different intensities of the turbulent velocity fluctuations, $\langle u^2 \rangle$. With the polystyrene particles acting as markers for the local flow velocities, experimental estimates can be obtained for the second-order structure function, $\Psi_2(y) = \langle (u_i(\mathbf{r}, t) - u_i(\mathbf{r} + \mathbf{y}, t))^2 \rangle$, being independent of t for stationary time conditions. An example is shown in figure 3, also including a fit for small separations given by a dashed line, using the universal Kolmogorov $(\epsilon r)^{2/3}$ law. If the separation vector is along the y-axis, we have the longitudinal structure function $\Psi_{2\parallel}(y) \equiv \langle (u_y(0, t) - u_y(y, t))^2 \rangle$ given by the dotted line, with C_K being the Kolmogorov constant, related to the spectral constant α from (2.1) by $C_K \approx 1.315\alpha$

(Monin & Yaglom 1975). We note that C_K is known with some uncertainty, and a value of $C_K \approx 2.5$ can be justified as well as $C_K \approx 2.0$ (Monin & Yaglom 1975; Ott & Mann 2000). The dash-dotted line in figure 3 gives the transverse structure function $\Psi_{2\perp}(y) \equiv \langle (u_x(0,t) - u_x(y,t))^2 \rangle$. By a general relation (Hinze 1975) we have

$$\Psi_{2\perp} = \frac{1}{2y} \frac{\mathrm{d}(y^2 \Psi_{2\parallel})}{\mathrm{d}y},$$

for locally homogeneous and isotropic turbulence. With $\Psi_{2\parallel} \approx C_K(\epsilon y)^{2/3}$, we find $\Psi_{2\perp} \approx (4/3)\Psi_{2\parallel}$ in the universal subrange. The solid line in figure 3 shows $\langle (u(r,t) - u(r+y,t))^2 \rangle = 2(\langle u^2 \rangle - \langle u(r,t) \cdot u(r+y,t) \rangle)$. The purpose of figure 3 is to demonstrate the existence of a universal range, and to indicate the range of its validity, here up to separations of the order of 20–25 mm, as determined by an approximately 20 % accurate fit to the assumed universal structure function. All lengths are measured in units of mm.

A large-scale mean flow can be observed in the experiment, with a velocity up to $5.3 \, \mathrm{mm \, s^{-1}}$ in the vertical direction, and $2.8\text{–}4.5 \, \mathrm{mm \, s^{-1}}$ in the two other directions, these values depending somewhat on the frequency of the grid oscillations (Mann *et al.* 1999). Other methods for forcing the turbulence (Webster, Brathwaite & Yen 2004; Hwang & Eaton 2004) may give smaller mean flows, but the resulting turbulence levels are often smaller as well. For the ensuing Lagrangian analysis, this large-scale motion is immaterial, but may imply a bias on the Eulerian results. The mean flow values should be compared to noticeably larger fluctuating velocities, see table 1.

2.1. *Spatial distributions of test particles*

The average distance between particles is much larger than their diameter, and particle interactions can be ignored. We estimate a Stokes number (Babiano *et al.* 2000) as $St \equiv (2/9)(a/\mathscr{L}_E)^2 R_e$ with R_e being the Reynolds number based on $\sqrt{\langle u^2 \rangle}$ and $\mathscr{L}_E$. For typical values (Ott & Mann 2000) of $\mathscr{L}_E = 25$ mm and $R_e \approx 500$ we find $St \approx 0.05 \ll 1$. To the given accuracy, we are therefore tempted to assume that the particles follow the flow as passive tracers (Maxey & Riley 1983). However, numerical results (Babiano *et al.* 2000) indicate that even for neutrally buoyant particles with small Stokes numbers, we can find non-trivial deviations between the local flow velocity and the particle velocity. This deviation seems to be manifested as an accumulation of particles in high-vorticity regions of the flow, i.e. an initially uniform spatial particle distribution becomes non-uniform with time. In the experiment, a fluid element spends a finite time between two consecutive encounters with the energizing grids, where the process, including the local re-distribution of particles, starts again. It is not *a priori* obvious whether this time is short enough to prevent significant particle accumulations.

In order to investigate the spatial distribution of particles, we make the hypothesis that for uniform particle distributions, the probability for finding a particle in a given volume element, $\mathrm{d}V$, is independent of the positions of all other particles, with the probability given by $P = \alpha \, \mathrm{d}V$, with α being a constant. It is well known that this assumption implies that the particles are distributed in space according to a Poisson distribution, which has the property that the standard deviation of the number N particles in a given volume V is $\langle N^2 \rangle - \langle N \rangle^2 = \langle N \rangle$. This is an easy relation to test experimentally. We show in figure 4 the distribution of the number of particles in a sphere with a given radius, and compare the result with the expected values for a Poisson distribution. In figure 5 we show the ratio $(\langle N^2 \rangle - \langle N \rangle^2)/\langle N \rangle$, and find that
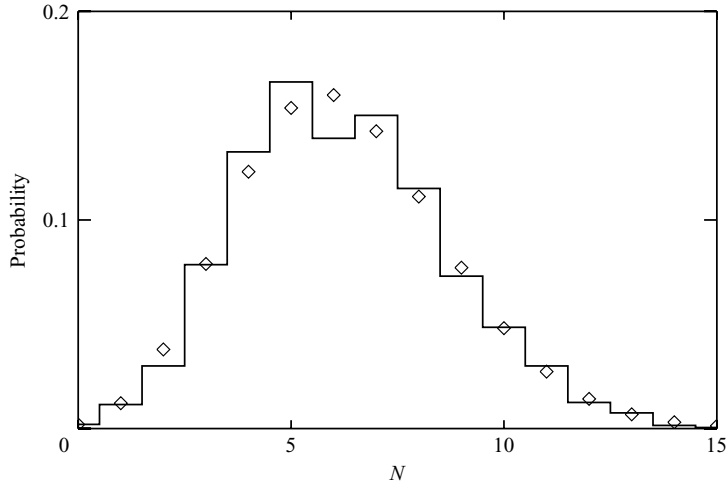
FIGURE 4. Statistical distribution of the number of particles in small spheres with radius $\mathscr{R} = 20\,\mathrm{mm}$. The symbol $\diamond$ gives the results obtained by assuming a Poisson distribution.
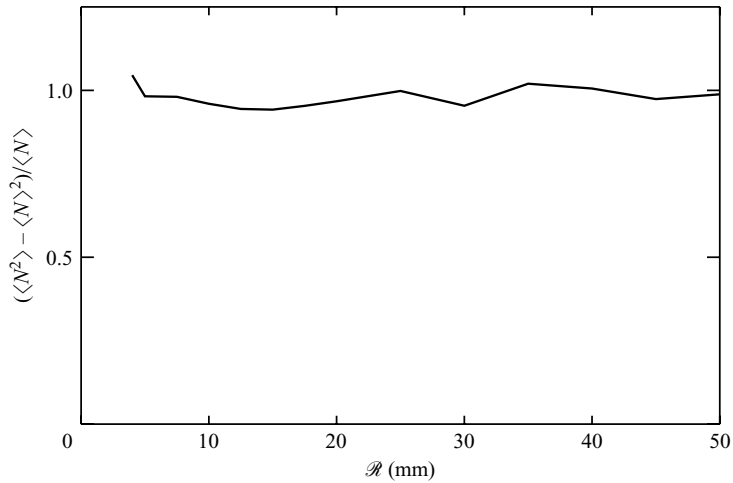

FIGURE 5. Test of the hypothesis $(\langle N^2 \rangle - \langle N \rangle^2)/\langle N \rangle = 1$ for a spatial Poisson distribution of particles, for various radii in spherical volume elements.

it is close to unity, as expected for a Poisson distribution. The relation is independent of the size and shape of the reference volume.

In the following we can therefore safely assume the particle density to be uniform, when interpreting fluxes to an absorbing surface. If we consider the spatial distribution of particle trajectories exceeding a prescribed length, the situation can, however, be different. If we consider the distribution of relatively short time traces (shorter than 1–1.5 s), we can also assume them to be uniformly distributed, with the exception of a small region at the boundaries of the measuring volume, see figure 1. If we, on the other hand, want to consider particle traces covering longer time intervals, we will find these to be non-uniformly distributed, with the largest concentration in the central region. The reason is simple: assume that a particle located close to the boundary marks the beginning of a sequence. If this particle moves inwards, it has
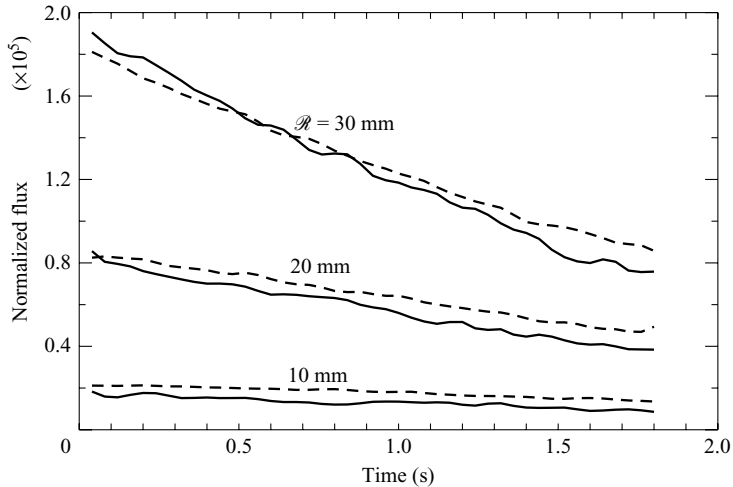
FIGURE 6. Time variation of the estimate for the averaged particle flux for unit density $\langle J(t) \rangle / n_0$, to stationary (dashed lines) and moving spheres (solid lines), with radii, $\mathscr{R} = 10$, 20 and 30 mm.

the possibility if being part of a long time sequence. If, on the other hand, it moves in the direction out of the measuring volume, the particle is likely to leave this volume and be lost, in the sense that it will no longer be detected. Consequently, the observed trace will be short in this latter case. A similar particle located close to the centre of the measuring volume will, on the other hand, have the possibility of marking the beginning of a long trace, irrespective of its direction of motion.

3. Particle flux into a stationary sphere

In this analysis, we select a reference sphere of interception with given radius, located at a fixed spatial position. At each time step, we remove all particles entering this fixed sphere in that time interval, and thus obtain an estimate for the particle flux. Evidently, there need not be any particle at the centre of the sphere for this Eulerian analysis. In figure 6 we show (with dashed lines) the averaged turbulent flux into stationary spheres, considering spheres with three different radii, where two are smaller than or comparable with the Eulerian length scale, while the third radius ($\mathscr{R} = 30$ mm) is larger. The absorption is, of course, virtual: the particles are physically still present, but for the subsequent analysis they are removed from the database after they have passed through the specified interception surface. When the analysis is repeated for a new position of the reference sphere, in order to improve the signal-to-noise ratio, or for a new choice of radius of the sphere, all particles are reintroduced in the database. This procedure is similar for the ensuing Lagrangian analysis, shown with a solid line in figure 6, to be discussed in detail in §4.

3.1. *Dimensional arguments*

For the Eulerian case considered here, we argue that the only characteristic velocity relevant for the problem is the root-mean-square velocity for the turbulent fluctuations, σ. As long as we consider only stationary reference spheres with radius $\mathscr{R}$ smaller than the characteristic length $\mathscr{L}_E$, we have a characteristic time $\mathscr{R}/\sigma$. Consequently, we expect that the normalized turbulent flux into the sphere can be written in the
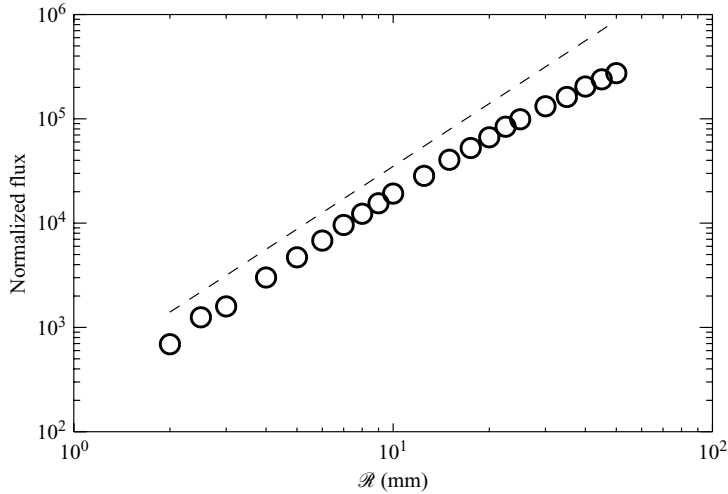
FIGURE 7. The normalized particle flux, $\langle J \rangle / n_0$, to a fixed stationary sphere of interception is shown with open circles for different radii, as measured at $1/2$ eddy turnover time, $t = \frac{1}{2}\tau_F$. The dashed line gives the $\mathscr{R}^2$-variation as a reference. Parameters are $\sigma = 19\,\text{mm}\,\text{s}^{-1}$, $\tau_F = 1.6\,\text{s}$, and $\epsilon = 225\,\text{mm}^2\,\text{s}^{-3}$. The fluxes are normalized to unit density.

form

$$\langle J \rangle / n_0 = \sigma \mathscr{R}^2 g(t\sigma/\mathscr{R}), \qquad (3.1)$$

since $\langle J \rangle$ has the dimension *time*$^{-1}$. We introduced the reference density of particles at $r \to \infty$ as n_0. As far as the dimensional analysis is concerned, g is an unknown dimensionless function, which, however, can be determined experimentally as in figure 6. For a simple diffusion equation in three dimensions, we find that the particle flux to an absorbing surface reaches a stationary level at large times, see for instance Appendix A. The observations summarized in figure 6 indicate that this is also the case for the present turbulent diffusion. In this stationary limit of g, the sole remaining parameter variation is that given by the coefficient $\sigma \mathscr{R}^2$ in (3.1).

In figure 7 we show the normalized particle flux to a stationary sphere of reference as obtained for different radii $\mathscr{R}$ of the spheres, all at a late time, here taken to be $\frac{1}{2}\tau_F$, defining $\tau_F \equiv \mathscr{L}_E/\sigma$ to be of the order of magnitude of an eddy turnover time. As a reference we inserted the simple $\mathscr{R}^2$-variation obtained by dimensional arguments, giving the coefficient of g in (3.1). A numerical coefficient is not accounted for.

The time-scaling postulated by (3.1) is also readily tested experimentally, with results shown in figures 8 and 9. In figure 9, for instance, we show the normalized flux into a stationary sphere, $\langle J \rangle / (n_0 \sigma \mathscr{R}^2)$, as a function of the normalized temporal variable, $t\sigma/\mathscr{R}$. The figure contains results from eight experimental conditions with different ϵ and σ, with parameters given in table 1. Each of these conditions was analysed for radii $\mathscr{R} = 5$, 6, 7, 8, 9, 10, 12.5, 15, 17.5, and 20 mm. Two different experimental conditions happened to give $\sigma = 12\,\text{mm}\,\text{s}^{-1}$ and $\sigma = 16\,\text{mm}\,\text{s}^{-1}$, and similarly two realizations were found for $\epsilon = 160\,\text{mm}^2\,\text{s}^{-3}$. Only radii in the universal subrange are considered in figures 8 and 9, i.e. $\mathscr{R} \leqslant 20\,\text{mm}$. The plotted curves have the same duration when measured in seconds, but due to the normalization, some will terminate at different normalized times. Figure 9 has a 'banded' structure, owing to two of the datasets (those with the two largest values of ϵ, see table 1) being somewhat different from the others. The simplest explanation for this observation
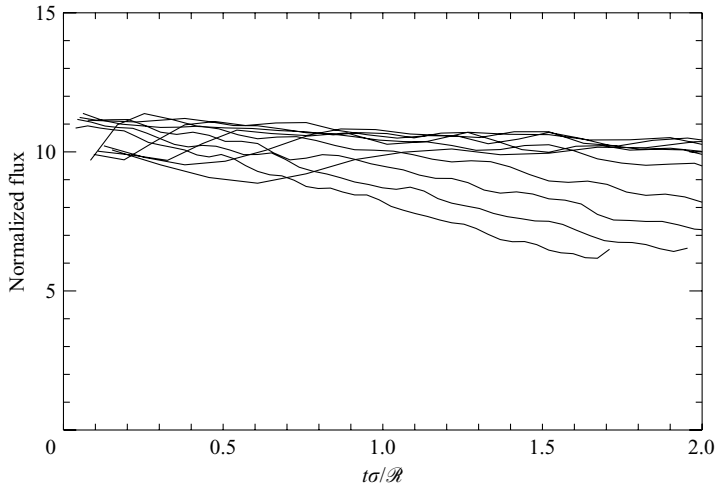
FIGURE 8. Normalized flux to a stationary spherical surface, $\langle J \rangle / (n_0 \sigma \mathscr{R}^2)$, as a function of the normalized temporal variable, $t\sigma/\mathscr{R}$, for a case where $\sigma = 19\,\mathrm{mm\,s^{-1}}$, $\tau_F = 1.6\,\mathrm{s}$, and $\epsilon = 225\,\mathrm{mm^2\,s^{-3}}$. The duration of the tracks measured in seconds is the same: in normalized time units, increasing $\mathscr{R}$ corresponds to successively shorter tracks.
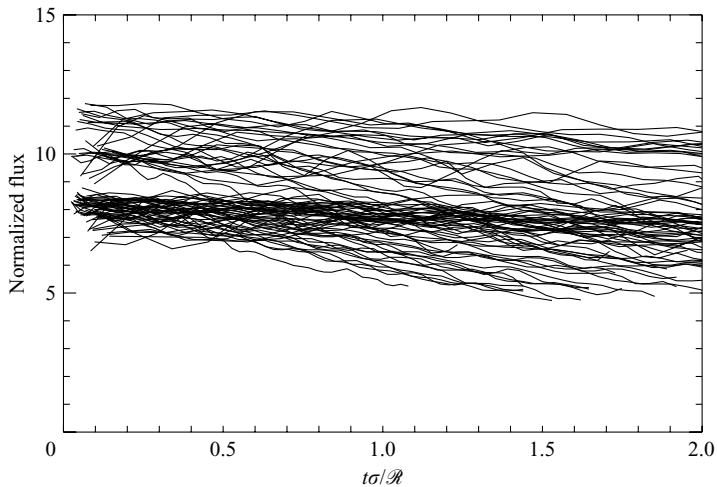

FIGURE 9. Normalized flux to a stationary spherical surface, $\langle J \rangle / (n_0 \sigma \mathscr{R}^2)$, as a function of the normalized temporal variable, $t\sigma/\mathscr{R}$. The figure contains results from eight experimental conditions.

might be that the experimental determinations of ϵ and σ are somewhat uncertain, and that this uncertainty affects the normalizations of the data in figure 9. For the present Eulerian analysis of the data, the small mean flow, mentioned before, can also have an effect.

For small radii, $\mathscr{R} \ll \mathscr{L}_E$, we find the scaling in (3.1) to be satisfied well. For increasing $\mathscr{R}$, the flux curves are consistently becoming lower. It can be concluded that the dimensional reasoning gives only fair agreement with observations. For fixed turbulence parameters, the scaling with $\mathscr{R}$ shown in figure 7 seems, however, to hold some promise.
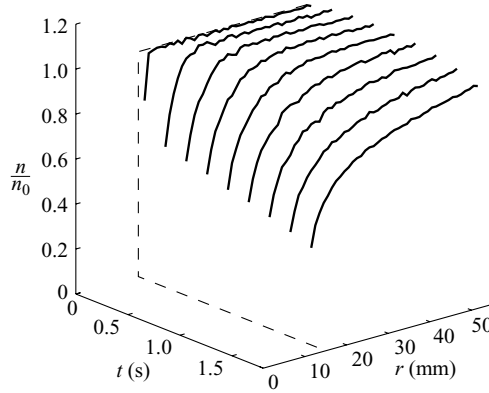
FIGURE 10. Time evolution of the normalized particle density around an absorbing stationary spherical surface, for $\mathscr{R} = 15$ mm. Parameters are as in figure 7.

As particles are absorbed by the surface, with particle flux densitites shown in figures 8 and 9, the particle density will be depleted in the flow surrounding the fixed reference spherical surface. We can analyse the average particle density for $r > \mathscr{R}$, as a function of time, with results shown in figure 10. The first curve shown is obtained at the first sample time, i.e. $t = 1/25$ s. Variations with distance are obtained in 'bins' of 1 mm, and the second bin from the surface at $r = \mathscr{R}$ is the first one shown. To reduce the noise level and to remove a density trend, we normalized the curves with the radial density variation found at $t = 0$.

It is evident that with a finite number of particles in the experiment, all or most of them will eventually be absorbed (in the sense discussed before): the system can obviously not be considered truly infinite. In all cases analysed, the time sequences are taken to be so short that at most 10 % of the particles are absorbed by the end of the corresponding analysis. This will be true also for the analysis of particle fluxes to a moving sphere.

4. Particle flux into a moving sphere

The foregoing Eulerian analysis can be repeated for the Lagrangian counterpart of the problem. With the records for simultaneous particle trajectories available, we can select one of them to represent the 'predator' and label all the others as 'prey'. We then select a predetermined radius $\mathscr{R}$ in the sphere of interception, and then remove all the particles which happen to be inside this sphere at the initial time. During the subsequent Lagrangian motion of the reference 'predator', we count the number of prey entering its co-moving sphere of interception between successive time steps. Each time a particle enters, it is 'eaten' in the sense that it is removed from the database. Of course, if the data analysis is carried out for very long times, all particles representing prey will eventually be removed. Here we are only interested in the time evolution of the prey flux for times up to an eddy turnover time. As long as $\mathscr{R}$ is much smaller than the size of the measuring volume, we can with negligible error assume the prey concentration to be constant at large distances, corresponding to an ideally infinite system. By choosing a large number of realizations, we can give an estimate for the ensemble-averaged Lagrangian prey flux as a function of time after release.

In figure 6 we show, with solid lines, examples of the time-varying particle flux to a moving sphere of interception with a given radius, $\mathscr{R}$. This flux is the result

of a competition between, on one hand, the depletion of the density of polystyrene particles in the near vicinity of the reference sphere as they are 'absorbed', and, on the other hand, inward flux of such particles, due to the turbulent motions in the flow. In each realization, we divide the flux by the particle density for that particular realization. The result thus represents the particle flux for unit particle density, i.e. 1 particle per mm^3. For small radii, $\mathcal{R} < \mathcal{L}_E$, we find that the flux level is almost constant in time. A decreasing trend becomes more conspicuous as the radius is increased, and for $\mathcal{R} > \mathcal{L}_E$ we find a significant flux reduction for times approaching the eddy turnover time, here estimated by $\tau_F \equiv \mathcal{L}_E/\sigma$. The flux is largest initially, when the concentration of 'prey' in the surroundings is largest. At later times there will be a possibility of encountering fluid elements which have already been emptied, and the prey flux becomes smaller. The flux depletion due to this effect evidently increases for increasing radii in the reference sphere.

To test the accuracy of the analysis, we have tried to omit the initially closest particle outside the sphere from the data analysis. The particle was omitted irrespective of its velocity. In particular for the smallest sphere radii, we found a clear decrease in the initial flux, as expected. For large radii, one missing particle did not make a significant difference.

5. Analytical results

The problem of turbulent particle flux to a perfect absorber moving with the flow can be studied analytically by making some simplifying assumptions. Here, an absorbing spherical surface is assumed to have its centre defined by a particle, which is moving with the flow.

5.1. *Dimensional arguments*

The present problem is characterized by a few dimensional quantities. With the viscosity, ν, being immaterial for the flow dynamics for scale lengths larger than the Kolmogorov length scale $\eta \equiv (\nu^3/\epsilon)^{1/4}$, we only have one quantity characterizing the flow, namely ϵ with dimension *length^2/time^3*, and the length scale $\mathcal{R} < \mathcal{L}_{int}$ characteristic for the particular problem, here a moving sphere of interception. Out of all these quantities the only combination giving a quantity with dimension *time* is $\mathcal{R}^{2/3}/\epsilon^{1/3}$, while $\epsilon^{1/3}\mathcal{R}^{7/3}$ gives *length^3/time*. The physical dimension of the averaged normalized particle flux $\langle J \rangle/n_0$ is *length^3/time*.

Quite generally it can then be argued, by purely dimensional reasoning, that the turbulent flux for given reference density n_0 must have the form

$$\frac{\langle J \rangle}{n_0} = \epsilon^{1/3}\mathcal{R}^{7/3} f\left(t\epsilon^{1/3}/\mathcal{R}^{2/3}\right), \tag{5.1}$$

with f being a dimensionless function of a dimensionless variable. The actual form of f can only be determined by a more detailed model analysis. We can argue that in figure 6, we have determined f experimentally, without reference to any explicit model equations. The arguments do not depend on any specific shape of the reference volume, and assume only that it scales self-similarly with one length scale, $\mathcal{R}$. The functional dependence f in (5.1) will, of course, be different for different shapes of the volume. Note that for $t > \mathcal{R}^{2/3}/\epsilon^{1/3}$, see figure 6, the variation of $f(\tau)$ is rather slow for parameters relevant here. The observations summarized in figure 6 seem to indicate that f approaches a constant value for large times. The constant is assumed to be universal, and we find it here to be in the range 5–10, as discussed in more

detail later. The observation is not as trivial as it might seem, see e.g. Appendix A and a discussion by Mann *et al.* (2003).

5.2. *A model diffusion equation*

The particle flux to a perfectly absorbing sphere which is moving with the flow has been modelled by, for instance, a simple diffusion equation with a properly chosen diffusion coefficient which depends on the simultaneous mean-square velocity differences obtained at given spatial separations, but independent of time (Osborn 1996). Essentially, the argument is based on the second-order structure function

$$\Psi_2(r) \equiv \langle (u_r(0, t) - u_r(r, t))^2 \rangle \approx C_K(\epsilon r)^{2/3}, \tag{5.2}$$

with the approximation being valid for separations r smaller than the length scale of the turbulence, see figure 3. A diffusion coefficient is constructed from a characteristic velocity and a characteristic length. The velocity is taken to be $\sqrt{\Psi_2(r)}$. For the limiting form expressed in (5.2), the only length characterizing the two particles is their separation r. The resulting diffusion coefficient is consequently $K(r) \sim r^{4/3}\epsilon^{1/3}$. The proposed diffusion equation for the density n is identical to the one suggested by Richardson in his study of distance-neighbour functions (Richardson 1926)

$$\frac{\partial}{\partial t}n(r, t) = C\frac{\epsilon^{1/3}}{r^2}\frac{\partial}{\partial r}r^{10/3}\frac{\partial}{\partial r}n(r, t). \tag{5.3}$$

The result is written for spherically symmetric geometry, with r being the radial coordinate, measured from the position of the centre of the reference sphere, and C is a numerical constant, assumed to be universal. While (5.3) was here obtained by dimensional reasoning, it also has an analytical derivation (Roberts 1961). As a consequence of (5.3) we have the well-known result for the mean-square separation of two initially close particles $\langle r^2 \rangle = C_R \epsilon t^3$, with the Richardson constant being $C_R \approx 0.5$ (Ott & Mann 2000). We have the relation $C = (3/2)(3C_R/143)^{1/3}$, giving $C \approx 0.33$. See Appendix B. In the present model, the time-varying diffusion flux of particles to a perfectly absorbing sphere is given by $4\pi C\epsilon^{1/3}\mathcal{R}^{10/3}\mathrm{d}n(r, t)/\mathrm{d}r|_{r=\mathcal{R}}$, with $n(r, t)$ obtained from (5.3).

The derivation of (5.3) assumes that ϵ is a deterministic constant, and thereby ignores intermittency corrections (Boffetta *et al.* 1999). Although relation (5.3) had some experimental support from the time when it was first proposed (Richardson 1926), and was also supported more recently (Ott & Mann 2000), its general validity has been criticized (Batchelor 1952; Roberts 1961), see also the summary by Ott & Mann (2000). The range of validity of (5.3) is not fully explored. For large separations, a simple diffusion equation, with constant diffusion coefficient, is expected to apply, as indicated for instance by experimental results (Virant & Dracos 1997), for initial conditions having scales larger than the integral length scale. These cases (Ott & Mann 2000; Virant & Dracos 1997) referred to particle releases considered as initial value problems. It seems that a diffusion equation as (5.3) can indeed be applied for analysing relative two-particle diffusion in certain ranges of variables (Ott & Mann 2000). On the other hand, one cannot expect a diffusion coefficient depending solely on relative times or spatial separations to be universally applicable for this problem (Roberts 1961). In general, a Fokker–Planck equation, with (5.3) being one special example, describes a Markov process, where the probabilities of future states depend solely on the present, and not past ones. Modelling of turbulent displacements as a simple Markov process is known to be rather inaccurate, and a study of the limits of applicability of models like (5.3) is therefore worthwhile.
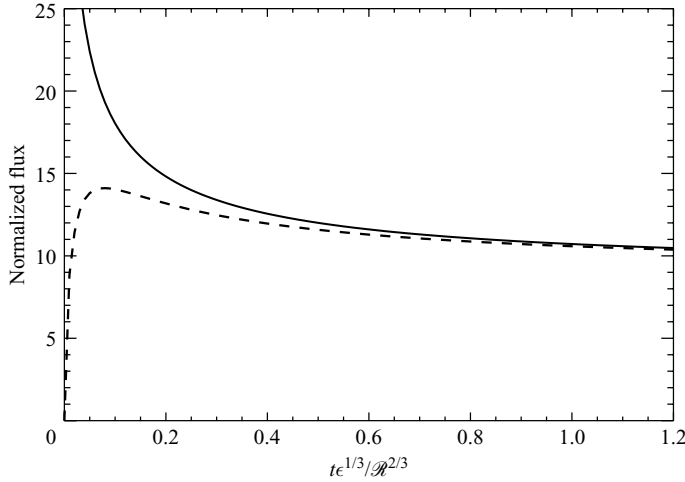
FIGURE 11. Time variation of the normalized flux, $\epsilon^{1/3}\mathcal{R}^{7/3}f(\tau = t\epsilon^{1/3}/\mathcal{R}^{2/3})$, obtained by numerical solutions of (5.3), for two initial conditions.

From (5.3) is easy to derive (Osborn 1996) a stead-state flux to a sphere with radius $\mathcal{R}$ as

$$\frac{J_0}{n_0} = \frac{28\pi}{3}C\epsilon^{1/3}\mathcal{R}^{7/3}, \qquad (5.4)$$

where n_0 is the constant particle density at $r \to \infty$, see also Appendix A. In figure 11 we show with solid line a numerical solution for the time-varying flux, using the normalized version of equation (5.3), where distance is normalized by $\mathcal{R}$ and time by $\mathcal{R}^{2/3}/\epsilon^{1/3}$. The flux to a sphere with unit radius in the normalized units is then calculated. The particle flux follows the normalizations obtained by the dimensional arguments in § 5.1. The (unphysical) singularity at $t = 0$ for the solid line solution is due to the assumed infinite initial gradient at $r = \mathcal{R}$.

The experimental uncertainty on particle positions (Mann *et al.* 1999) is approximately 0.02 mm. The idealized step function in particle density, assumed as an initial condition when obtaining the solid line solution in figure 11, is therefore not necessarily a correct representation for our experimental conditions. To illustrate the dependence on this initial variation of the density, we also show in figure 11 by a dashed line the flux for a case where the initial density condition is $1 - \exp(-(r - \mathcal{R})^2/\Delta^2)$ for $r > \mathcal{R}$, and vanishing otherwise. This model is feasible for representing a 'smearing out' of the initial density gradient due to the uncertainty in particle positions. We used a relatively large value $\Delta = 0.25\mathcal{R}$ as an illustration. In this case, the singularity of the initial condition has been removed, but a peak in the calculated flux is still clearly noticeable. We find that the uncertainty associated with the particle positions will have little relevance for our data analysis, as far as the model equation (5.3) is concerned.

5.3. Comparison between analytical and experimental results

In order to compare our observations with analytical results, we show by open circles in figure 12 the flux value at a time $t = \frac{1}{2}\tau_F$, with τ_F being the eddy turnover time. This time is sufficiently short to give a large number of particle traces for the averaging, and on the other hand, sufficiently long to give an estimate close to the asymptotic flux value of the particle flux. Vertical lines give the uncertainties on the experimental
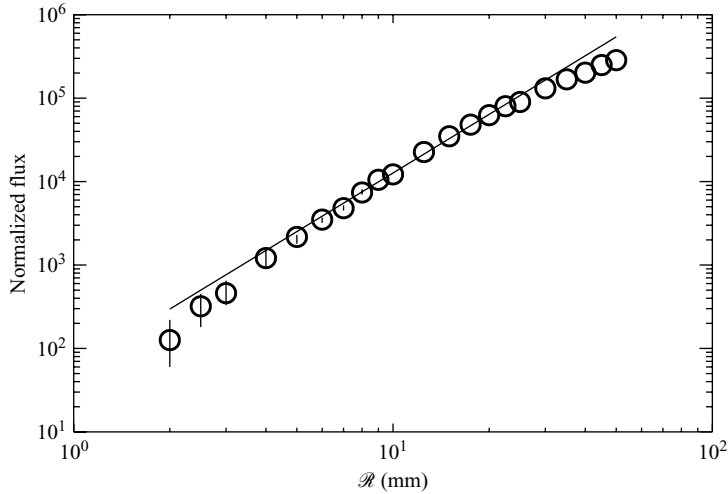
FIGURE 12. The particle flux, $\langle J \rangle/n_0$, to a moving sphere of interception is shown with open circles for different radii, as is measured at $1/2$ eddy turnover time, $t = \frac{1}{2}\tau_F$. The solid line gives the time-asymptotic result (5.4). Parameters are $\sigma = 19\,\mathrm{mm\,s^{-1}}$, $\tau_F = 1.6\,\mathrm{s}$, and $\epsilon = 225\,\mathrm{mm^2\,s^{-3}}$. The fluxes are normalized to unit density.

estimates. For small radii $\mathscr{R}$, this uncertainty is large because we seldom find close particles. For $\mathscr{R} > 5\,\mathrm{mm}$, on the other hand, this uncertainty is smaller than the size of the circles in figure 12. The analytical curve, given by a solid line, is the asymptotic limit from (5.3), where we used $\epsilon = 225\,\mathrm{mm^2\,s^{-3}}$. Taking into account that we have not introduced any free or adjustable parameters, we find the agreement between the analytical and experimental results to be satisfactory, although we note a slight, but systematic, reduction of the measured flux compared with the analytical asymptotic result. The experimental results for the smallest radii give an underestimate, since in this limit a non-trivial fraction of the particles are 'glancing', i.e. they pass through the reference sphere within one sampling time, and are therefore not counted.

The model equations become inadequate for spatial separations larger than the largest eddies in the turbulence, $r \geqslant \mathscr{L}_E$, although we find that the $\mathscr{R}^{7/3}$-scaling seems to have a wider range of validity, in particular at early times, $t < \frac{1}{2}\tau_F$. The analysis summarized here refers explicitly to spherical volumes. Qualitatively, the arguments will apply to different shapes as well, as long as they scale self-similarly with one characteristic length, $\mathscr{R}$.

We also present results for the flux variation for a fixed value of the radius of the moving sphere of interception, $\mathscr{R} = 20\,\mathrm{mm}$, and varying ϵ, see figure 13. In order to sample each dataset at a consistent time, we present results for a selected time $\frac{1}{2}\tau_F$ used also in figure 12, with the appropriate value of σ. In this limit, we can in all cases assume that the particle flux is close to its asymptotic, or saturated, level. The circles show the result for ϵ obtained by fitting the second-order structure function. Other methods for determining ϵ can be found, however (Mann *et al.* 1999), and these results are used to give the horizontal uncertainty bars. The theoretical solid line is also in this case obtained as the asymptotic limit of the solution of Richardson's diffusion equation, using the most recent experimental value (Ott & Mann 2000) of Richardson's constant. Within the range of variability, we find the scaling with ϵ to agree reasonably well with theoretical predictions based on (5.3). The numerical
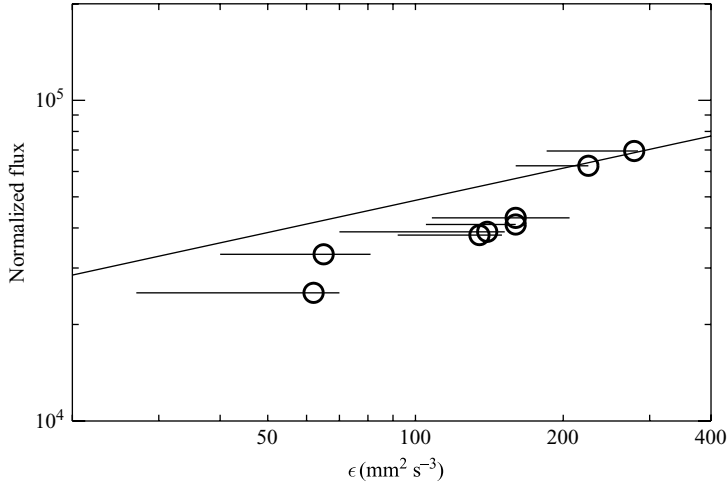
FIGURE 13. Variation of the normalized flux, $\langle J \rangle / n_0$, with varying ϵ for a fixed value of $\mathscr{R} = 20$ mm. The solid line gives the time-asymptotic result obtained from (5.3). See also figure 12.

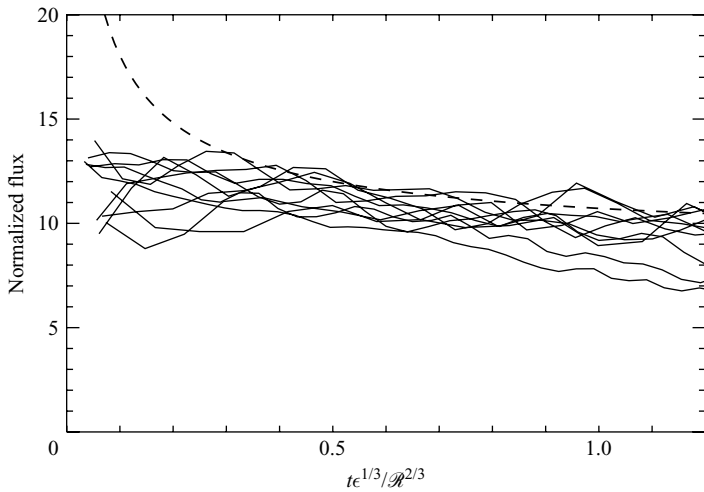
FIGURE 14. Normalized flux, $\langle J \rangle / (n_0 \epsilon^{1/3} \mathscr{R}^{7/3})$, as a function of the normalized temporal variable, $t\epsilon^{1/3}/\mathscr{R}^{2/3}$, for various radii and $\epsilon = 225$ mm^2 s^{-3}. The dashed line gives a theoretical result, obtained from (5.3), see also figure 11.

agreement between the measurements and analytical results is within a factor of 2, the analysis predicting a slightly larger flux than the observed value, also in agreement with the results shown in figure 12. The selected value $\mathscr{R} = 20$ mm can be taken as representative of the length scales smaller than or equal to $\mathscr{L}_E$ in the experiments.

The results summarized in figures 12 and 13 refer to fluxes obtained at fixed normalized times. We can also demonstrate a scaling law for the time variations of these fluxes, and compare the results to the results from the model as illustrated in figure 11. In figure 14 we show the normalized flux variation as function of normalized time, for one set of experimental conditions, $\epsilon = 225$ mm^2 s^{-3} and $\sigma = 19$ mm s^{-1}, and radii $\mathscr{R} = 5$, 6, 7, 8, 9, 10, 12.5, 15, 17.5 and 20 mm. These values are chosen to be small enough to be within the universal subrange, but sufficiently large to give modest
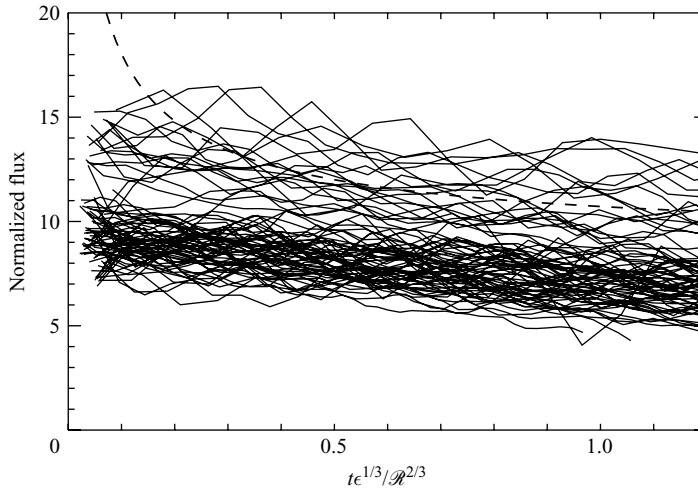
FIGURE 15. Normalized flux, $\langle J \rangle/(n_0 \epsilon^{1/3} \mathcal{R}^{7/3})$, as a function of the normalized temporal variable, $t\epsilon^{1/3}/\mathcal{R}^{2/3}$. Curves are shown for eight realizations with different turbulence conditions, as in figure 9, each with curves for different $\mathcal{R}$. The dashed line gives a theoretical result, obtained from (5.3), see also figure 11.

statistical uncertainty in the estimate. In figure 15 we show the normalized fluxes for eight different experimental conditions, see table 1, using the same radii, $\mathcal{R}$, as in figure 14. The figure demonstrates an experimental scatter, which is consistent with the uncertainties in the estimates for ϵ. Also here we note a 'banded' structure in the figure, although not as pronounced as in figure 9. We find that the uppermost group of curves originates from the two datasets with the largest ϵ-values, see for instance also figure 13, where these two datasets also seem to be slightly distinct from the others. Ideally, we expect that the curves should all collapse into one, and found no systematic variation with parameters, apart from the the two values of ϵ, as already mentioned.

Again, we note that the results have a wider range of applicability, and need not refer explicitly to spherical forms. A change in the shape of the reference volume, will only imply a change in the numerical constant. Thus, the scaling law implied in figure 13 will apply, for instance, to the prey flux for any predator, independent of the shape of the interception volume, when it is exposed to different turbulence intensities.

Given the experimental uncertainties, the scaling relations obtained by dimensional reasoning are found to be satisfied well when analysing the data from our experiment. The more specific diffusion equation model (5.3) only gives qualitative agreement for the measured Lagrangian fluxes at early times. It seems, however, that the asymptotic limit is accounted for well by the model, in particular also the numerical coefficient obtained by use of the most recent value of the Richardson constant (Ott & Mann 2000).

As particles are absorbed by the surface, with fluxes shown in figures 14 and 15, the particle density will be depleted in the flow surrounding the moving reference sphere. We can also analyse here the average particle density for $r > \mathcal{R}$, as a function of time, with results shown in figure 16. The radius $\mathcal{R}$ is chosen to be in the universal subrange. The first curve is shown at the first sampling time, i.e. $t = 1/25$ s. Variations with distance are obtained in 'bins' of 1 mm, and the second bin from the surface at $r = \mathcal{R}$ is
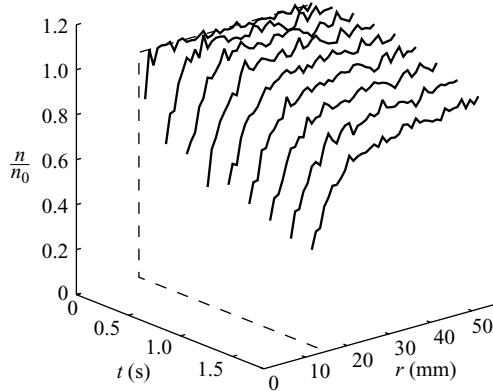
FIGURE 16. Time evolution of the normalized density around an absorbing spherical surface moving with the flow, for $\mathscr{R} = 15$ mm. Parameters are as in figure 7.

the first one shown. To reduce the noise level, we also normalized here the curves with the radial density variation found at $t = 0$. The present results can be compared with the corresponding figure for the stationary surface, see figure 10. Unfortunately, with the present noise level, it is difficult to demonstrate a significant quantitative difference between the Eulerian and Lagrangian density variations, although the physical conditions are very different in the two cases. If we choose a smaller value for $\mathscr{R}$, the noise level increases, while larger $\mathscr{R}$ will fall outside the universal subrange. For these large radii, the differences between the particle densities surrounding stationary and the moving absorbing spheres become conspicuous, in particular for large t and r. By closer inspection, we find that the gradient in the average density, as measured just outside the absorbing sphere, is steepest for the Eulerian case.

6. Conclusions

In this paper we investigate the turbulent flux to a perfectly absorbing surface, with particular attention paid to the problem of predator–prey encounters in turbulent flows. We have summarized the basic elements of an experimental method for investigating the prey flux to a moving predator. In the limit of small $\mathscr{R}$, we found evidence for an $\mathscr{R}^{7/3}$ flux scaling (see figure 12) in terms of the radius of the sphere of interception. We also found indications of an $\epsilon^{1/3}$ scaling with the turbulent dissipation rate (see figure 13), in agreement with the predictions of the model equation (5.3). This model also agrees to some extent quantitatively with the observations. In the asymptotic time limit, to the extent it can be reached in the present experiment, the data give a flux approximated well by (5.4), provided $\mathscr{R} < \mathscr{L}_E$. This will in general be the limit relevant for marine environments (Hill, Nowell & Jumars 1992). We assume that the observations justify extrapolation to radii, $\mathscr{R}$, smaller than those experimentally accessible. In a general sense, our results also provide experimental evidence for the importance of turbulent motion for the feeding process in marine environments. We expect that in order to obtain a general analytical model, which can give results for extended time periods and all $\mathscr{R}$, we will have to allow for a diffusion coefficient which depends on time as well as spatial separations, in particular also including memory effects (Roberts 1961; Borgas & Yeung 2004).

The turbulent flux to a moving sphere can be significantly smaller than the flux to a stationary one. This can be argued simply by noting that the relative mean-square
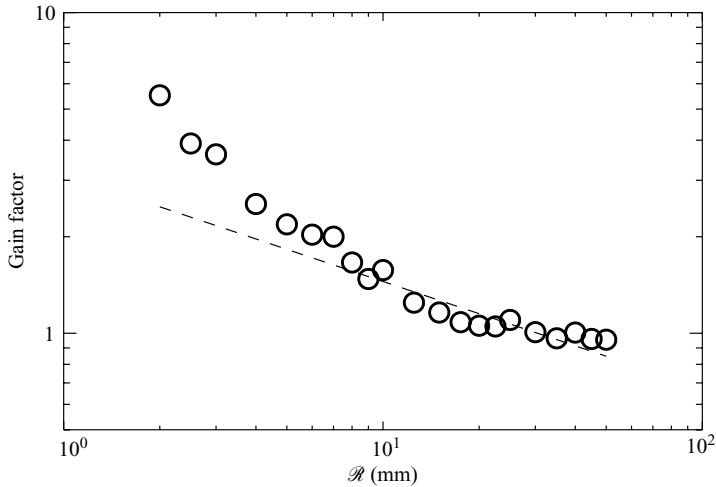
FIGURE 17. Variation of the gain factor for a stationary sphere for various radii of the sphere of interception, $\mathscr{R}$. The figure refers to a time $t = \frac{1}{2}\tau_F$.

velocity of a particle convected past a stationary sphere is $\langle u^2 \rangle$, while it is $\langle(\boldsymbol{u}(\boldsymbol{r}, t) - \boldsymbol{u}(\boldsymbol{r} + \boldsymbol{y}, t))^2\rangle$, for a passively convected sphere–particle pair, with separation $\boldsymbol{y}$. For small separations, $y \ll \mathscr{L}_E$, we have (Chandrasekhar 1957; Osborn 1996) the result (5.2), and the relative velocity is small, implying a small flux to the passively convected sphere. For large separations, $y \gg \mathscr{L}_E$, on the other hand, $\boldsymbol{u}(\boldsymbol{r}, t)$ and $\boldsymbol{u}(\boldsymbol{r} + \boldsymbol{y}, t)$ can be supposed to be statistically independent. The mean-square relative velocity is then $2\langle u^2 \rangle$. The flux in this latter case is expected to be larger than that to the stationary sphere with a factor $\sqrt{2}$, although such large separations cannot be achieved for the present experimental conditions.

We can define a 'gain factor' as the ratio between the flux to a stationary sphere and the flux to the passively convected sphere with the same radius, $\mathscr{R}$. In figure 17 we show this gain factor for various radii, $\mathscr{R}$. All points are obtained at the reference time $\frac{1}{2}\tau_F$ used before. We find that the gain factor is considerable for small spheres of interception, using the length scale $\mathscr{L}_E$ as a measure. For $\mathscr{R} \approx \mathscr{L}_E$ this gain factor is close to 1, and the particle flux is the same for a stationary as for the moving sphere. For larger values, $\mathscr{R} > \mathscr{L}_E$, the flux to a moving sphere exceeds that to a stationary one. The variation of the initial value of the fluxes seen, for instance, on figure 6 is consistent with these observations. Heuristically, we can argue for a parameter variation of the gain factor as given by the ratio of the two scaling laws obtained by dimensional arguments, which here gives $\sigma/(\epsilon\mathscr{R})^{1/3}$. This ratio is shown by a dashed line in figure 17, with a numerical constant not accounted for. We find, in this case, that this scaling law does not follow the data points in any convincing way, although the trend seems reasonable. After all, neither the Eulerian nor the Lagrangian data followed the scaling perfectly, the Eulerian data best at small $\mathscr{R}$, the Lagrangian data best at somewhat intermediate values. To expect a perfect agreement for the ratio of the two quantities may seem somewhat optimistic, in particular because the mean flow in the system gives a bias for the Eulerian fluxes. The gain factor shown in figure 17 can, for instance, be interpreted as the gain in prey flux for an imagined predator with possibilities for self-induced motion, which it uses to exactly compensate the motions in the surrounding water.

The problem discussed here is clearly of general interest. It has implications for coagulation processes in turbulent colloids, for instance. A detailed investigation of this latter problem cannot, however, be made by experiments like ours because the volume of the particles change upon coagulation, with a consequent change in their response to the turbulent flow motions. We cannot reproduce this effect, for obvious reasons. In standard studies of this problem (Chandrasekhar 1954), restricted to diffusion by Brownian motion, this effect is in part also ignored. With the same assumption it is possible to perform the relevant studies in experiments like ours, with results having implications for the formation rate of coagulants larger than the Kolmogorov scale η in turbulent flows.

Appendix A. Simple models for the saturated turbulent flux

Consider a diffusion equation of the form

$$\frac{\partial}{\partial t} P(r, t) = \frac{1}{r^{d-1}} \frac{\partial}{\partial r} r^{d-1} K(r) \frac{\partial}{\partial r} P(r, t) \qquad (A\,1)$$

where $P(r, t)$ is the ensemble-averaged particle density, being related to the distance-neighbour function introduced by Richardson (1926). Here, d is the dimensionality of the problem, while $K(r)$ is a diffusion coefficient depending on r, but otherwise unspecified for the moment. The expression (5.3) corresponds to $d = 3$ and $K(r) \sim r^{4/3}$.

We solve (A 1) for the case where we have an absorbing boundary at $r = \mathcal{R}$, i.e. with $P(\mathcal{R}, t) = 0$. To have a steady-state solution for (A 1), we obviously require the left-hand side to vanish, implying that

$$r^{d-1} K(r) \frac{\mathrm{d}}{\mathrm{d}r} P(r) = \text{const.}$$

The constant can be determined by $P(r \to \infty) = n_0$, which is assumed known. We have

$$P(\infty) - P(\mathcal{R}) = \int_{\mathcal{R}}^{\infty} \frac{\mathrm{d}}{\mathrm{d}r} P(r) \, \mathrm{d}r = \int_{\mathcal{R}}^{\infty} \frac{\text{const}}{r^{d-1} K(r)} \, \mathrm{d}r$$

or

$$\text{const} = \frac{n_0}{\displaystyle\int_{\mathcal{R}}^{\infty} \frac{\mathrm{d}r}{r^{d-1} K(r)}}.$$

The time-stationary diffusion flux of particles to a perfectly absorbing sphere is given by $J_0 = \pi(2\mathcal{R})^{d-1} K(r) \mathrm{d}P(r)/\mathrm{d}r|_{r=\mathcal{R}}$, in the negative r-direction, towards the spherical surface. We find

$$\frac{J_0}{n_0} = \frac{\pi 2^{d-1}}{\displaystyle\int_{\mathcal{R}}^{\infty} \frac{\mathrm{d}r}{r^{d-1} K(r)}}, \qquad (A\,2)$$

where π is to be omitted in the one-dimensional case.

Hitherto, we have not specified the diffusion coefficient $K(r)$. The Richardson model (Richardson 1926) has $K = C\epsilon^{1/3}r^{4/3}$, including a universal constant, C. Using this model for a three-dimensional case, we find

$$\frac{J_0}{n_0} = C\,\frac{4\pi\epsilon^{1/3}}{\displaystyle\int_{\mathscr{R}}^{\infty}\frac{\mathrm{d}r}{r^{10/3}}} = \frac{28\pi}{3}\,C\epsilon^{1/3}\mathscr{R}^{7/3}.$$

In two spatial dimensions we find $J_0/n_0 = (8\pi/3)C\epsilon^{1/3}\mathscr{R}^{4/3}$. We note that for a diffusion equation with constant diffusion coefficient, $K(r) = D$, the two-dimensional case is singular, by giving a logarithmically diverging integral in (A 2). Consequently, non-trivial stationary flux limits do not exist for this case (Mann *et al.* 2003). A simple diffusion equation for three spatial dimensions has a saturated normalized flux $J_0/n_0 = 4\pi D\mathscr{R}$, as readily obtained from (A 2).

Appendix B. Methods for determining the Richardson constant

When discussing methods for determining the Richardson constant, Boffetta *et al.* (1999) and Boffetta & Sokolov (2002) noted a problem associated with the straightforward idea of following a large number of initially close particle pairs, and subsequently determining their mean-square average separation as function of time. If an experimental study of relative diffusion is attempted for realistic experimental or numerical conditions, a problem arises because of the finite size of the inertial, or universal, subrange. To obtain the numerical constant, C_R, appearing in Richardson's law for relative mean-square particle separations, experimentally (Mann *et al.* 1999; Ott & Mann 2000) or numerically (Boffetta *et al.* 1999; Boffetta & Sokolov 2002), a large number of realizations is needed in order to estimate the average value $\langle r^2(t)\rangle$. Even for short times, a significant number of particle pairs entering this average will, however, have a separation which is large and outside the universal subrange. This 'cross-over' effect can be avoided by considering a fixed spatial scale within the universal subrange, and instead taking the average time $\langle t \rangle$ associated with this scale. It is evident that the numerical constant obtained this way is specific for the fixed scale problem. It was demonstrated (Boffetta *et al.* 1999; Boffetta & Sokolov 2002), that this constant can be related to the fixed time problem by use of Richardson's diffusion equation (Richardson 1926). It was suggested that the average time for particles initially located at a sphere with radius $\mathscr{R}_1$ to reach a shell with radius $\mathscr{R}_2 > \mathscr{R}_1$ could be measured and used to express C_R. The applicability of the scheme was demonstrated numerically, and good agreement was found with experimental values for C_R. We have only been able to reproduce the numerical value for C_R by this method applied to our data, by careful choice of the ratio $\mathscr{R}_1/\mathscr{R}_2$. We should like to point out that the saturated flux to an absorbing sphere considered here can be used as well, and perhaps even more easily, for similar investigations. Also in this case, the scale is uniquely given by the radius of the sphere and the particle flux, where the density at infinity has to be given. This formulation of the problem contains exactly the same information as the scale-method suggested by Boffetta *et al.* (1999) and Boffetta & Sokolov (2002). There remains one basic distinction between using $\langle r^2(t)\rangle$ directly (as done by Ott & Mann 2000), as compared with the scale methods, namely that the former case is model independent, while the latter relies on an *a priori* given diffusion equation, with a questionable range of validity.

REFERENCES

BABIANO, A., CARTWRIGHT, J. H. E., PIRO, O. & PROVENZALE, A. 2000 Dynamics of a small neutrally buoyant sphere in a fluid and targeting in Hamiltonian systems. *Phys. Rev. Lett.* **84**, 5764–5767.

BATCHELOR, G. K. 1952 Diffusion in a field of homogeneous turbulence II. The relative motion of particles. *Proc. Camb. Phil. Soc.* **48**, 345–362.

BOFFETTA, G., CELANI, A., CRISANTI, A. & VULPIANI, A. 1999 Pair dispersion in synthetic fully developed turbulence. *Phys. Rev.* E **60**, 6734–6741.

BOFFETTA, G. & SOKOLOV, I. M. 2002 Relative dispersion in fully developed turbulence: the Richardson law and intermittency corrections. *Phys. Rev. Lett.* **88**, 094501.

BORGAS, M. S. & YEUNG, P. K. 2004 Relative dispersion in isotropic turbulence. Part 2. A new stochastic model with Reynolds-number dependence. *J. Fluid Mech.* **503**, 125–160.

CHANDRASEKHAR, S. 1954 Stochastic problems in physics and astronomy. In *Selected Papers on Noise and Stochastic Processes* (ed. N. Wax), pp. 3–91. Dover.

CHANDRASEKHAR, S. 1957 The theory of turbulence. *J. Madras Univ.* B **27**, 251–275.

HILL, P. S., NOWELL, A. R. M. & JUMARS, P. A. 1992 Encounter rate by turbulent shear of particles similar in diameter to the Kolmogorov scale. *J. Mar. Res.* **50**, 643–668.

HINZE, J. O. 1975 *Turbulence*, 2 edn. McGraw-Hill.

HWANG, W. & EATON, J. K. 2004 Creating inhomogeneous and isotropic turbulence without a mean flow. *Exps. Fluids* **36**, 444–454.

KIØRBOE, T. & SAIZ, E. 1995 Planktivorous feeding in calm and turbulent environments, with emphasis on copepods. *Mar. Ecol. Prog. Ser.* **122**, 135–145.

MANN, J., OTT, S. & ANDERSEN, J. S. 1999 Experimental study of relative, turbulent diffusion. *Tech. Rep.* Risø-R-1036(EN). Risø National Laboratory, DK-4000 Roskilde, Denmark. Can be downloaded from http://www.risoe.dk/rispubl/VEA/ris-r-1036.htm.

MANN, J., OTT, S., PÉCSELI, H. L. & TRULSEN, J. 2002 Predator-prey encounters in turbulent waters. *Phys. Rev.* E **65**, 026304.

MANN, J., OTT, S., PÉCSELI, H. L. & TRULSEN, J. 2003 Experimental studies of occupation times in turbulent flows. *Phys. Rev.* E **67**, 056307.

MAXEY, M. R. & RILEY, J. J. 1983 Equation of motion for a small rigid sphere in a nonuniform flow. *Phys. Fluids* **26**, 883–889.

MONIN, A. S. & YAGLOM, A. M. 1975 *Statistical Fluid Mechanics*, Vol. 2. The MIT Press.

MUELBERT, J. H., LEWIS, M. R. & KELLEY, D. E. 1994 The importance of small-scale turbulence in the feeding of herring larvae. *J. Plankton Res.* **16**, 927–944.

OSBORN, T. 1996 The role of turbulent diffusion for copepods with feeding currents. *J. Plankton Res.* **18**, 185–195.

OTT, S. & MANN, J. 2000 An experimental investigation of the relative diffusion of particle pairs in three dimensional turbulent flow. *J. Fluid Mech.* **422**, 207–223.

RICHARDSON, L. F. 1926 Atmospheric diffusion shown as a distance-neighbour graph. *Proc. R. Soc. Lond.* A **6**, 709–737.

ROBERTS, P. H. 1961 Analytical theory of turbulent diffusion. *J. Fluid Mech.* **11**, 257–283.

ROTHSCHILD, B. J. & OSBORN, T. R. 1988 Small-scale turbulence and plankton contact rates. *J. Plankton Res.* **10**, 465–474.

SUNDBY, S. & FOSSUM, P. 1990 Feeding conditions of arcto-norwegian cod larvae compared with the Rothschild-Osborn theory on small-scale turbulence and plankton contact rates. *J. Plankton Res.* **12**, 1153–1162.

VIRANT, M. & DRACOS, T. 1997 3D PTV and its application on Lagrangian motion. *Meas. Sci. Technol.* **8**, 1529–1552.

WEBSTER, D. R., BRATHWAITE, A. & YEN, J. 2004 A novel laboratory apparatus for simulating isotropic oceanic turbulence at low Reynolds number. *Limnol. Oceanogr. Meth.* **2**, 1–12.